SPE Journal

SJ-0824-0062

# Geochemical Impact of Acid Spearhead and Slick Water Stimulation on Wolfcamp Shale from the Hydraulic Fracturing Test Site

**Wei Xiong[1,2]*; Hang Deng[3]; Mengling Stuckman[1]; Adam Jew[4]; Johnathan Moore[5]; Dustin Crandall[5]; Christina Lopano[1]; J. Alexandra Hakala[1]**

[1]National Energy Technology Laboratory, Pittsburgh, PA 15236, USA
[2]NETL Support ContractorPittsburgh, PA 15236, USA
[3]Peking University, Beijing, 100871, China
[4]Stanford Synchrotron Radiation Lightsource, SLAC National Accelerator Laboratory, Menlo Park, CA 94025, USA
[5]National Energy Technology Laboratory, Morgantown, WV 26505, USA

*Corresponding author; email: wei.xiong@netl.doe.gov

## ABSTRACT

The Hydraulic Fracturing Test Site 1 (HFTS-1) was a field study performed in the Wolfcamp Formation in the West Texas Permian (Midland) Basin, USA with a focus on improving the efficiency of hydraulic fracturing. Investigating site-specific rock-fluid geochemical interactions during hydraulic fracturing is an important step to understand the impact on formation shale porosity, permeability, and long-term shale gas production. During field operations in this region, hydraulic fracturing fluid (HFF) injection usually starts with a concentrated acid spearhead for rapid rock dissolution, followed by the injection of near-neutral pH slick water containing chemicals and proppants. A multi-step sequential injection approach was used to investigate different stages of rock-fluid interactions. The carbonate content in the host rock is important when acid spearhead is considered, as carbonate mineral dissolution is rapid and can result in porosity and permeability changes in the shale matrix. In this study, we designed flow-through experiments using fractured carbonate-rich and clay-rich Wolfcamp shale cores with 1) a short-time acid soaking step and 2) a long-term slick-water flow-through step to simulate the injection method used at HFTS-1. The fluid chemistry was analyzed. A thorough mineralogical progression (e.g., Ca dissolution and Fe redox progression) in the cores during HFF injection was also characterized and imaged by synchrotron microprobe. Reactive transport modeling was performed based on the experimental setup. The results showed that the acid spearhead is a crucial step to create reaction front by mineral dissolution, especially in carbonate-rich shales. A slight layer of ferrihydrite precipitated during the slick-water flow-through period. This study provided insights on potential geochemical impact due to hydraulic fracturing operations in Permian Basin.

## 1. INTRODUCTION

Hydraulic fracturing is a technique to increase rock permeability for gas and oil extraction by injecting large volumes of hydraulic fracturing fluid (HFF) into deep shale reservoirs (Chen and Carter, 2017; U.S.EPA, 2015; Vidic et al., 2013). The HFF usually contains proppants and a series of chemical additives including acid to facilitate the fracturing process and promote mineral dissolution (U.S.EPA, 2015). Shale-HFF geochemical interactions have great impact on the fluid chemistry and mineral dissolution/precipitation during hydraulic fracturing. The geochemical impact can vary significantly depending on the mineralogy of the shale formations and the chemistry of the injected HFF. It is important to study site-specific geochemistry based on target basin mineralogy, water chemistry and injecting methods.

The Hydraulic Fracturing Test Site 1 (HFTS) was a field-based hydraulic fracturing research experiment performed in the Wolfcamp Formation in the West Texas Permian (Midland) Basin (Ciezobka et al., 2018). During operations in this region, an acid spear head was generally applied for a short period before injecting the slick water into the shale to pretreat the rocks to increase permeability and porosity (Khan et al., 2021). Shale-acid reactions are quick and intense (Wang et al., 2020). The exposed shale surface and the fluid can

be chemically altered, even though the acid spear head is usually very short (within minutes) compared to the entire hydraulic fracturing process (days to weeks). The initial acid exposure may affect the subsequent interactions with the slick water. The rock-fluid interactions can lead to the release of organic and inorganic contaminants that can be challenging for produced water management (Balaba and Smart, 2012; Field et al., 2014; Flynn et al., 2019; Haluszczak et al., 2013; Harrison et al., 2017).

Mineral composition of the shale is another important factor influencing the shale-HFF geochemical interactions, especially considering the acid exposure. Certain formations can be stimulated by the HFF resulting in much larger induced permeability than other formations with the same HFF (Thompson and DeVine, 1995). In Wolfcamp shale with abundant calcium carbonate, acid spearheads can promote enhanced porosity to an extent that new mineral precipitation has little effect on reducing any newly generated permeability (Jew and Brownlow, 2025). In a prior experimental study, carbonate in Marcellus and Barnett shales was fully dissolved, while Eagle Ford and Green River shales still contained a significant amount of carbonates even after 6 months of reaction (Jew et al., 2017). In low-carbonate Marcellus shale, a pyrite ($FeS_2$) oxidation zone was observed in the reaction front (Li et al., 2019). Carbonate dissolution increased the porosity at the shale-HFF interface, and the thickness of the dissolution front varied with Marcellus shale and Eagle ford shale (Li et al., 2019). Barite precipitates could reduce the permeability in clay-rich Marcellus shale, while the carbonate-rich Eagle Ford shale showed an order of magnitude increase in permeability due to carbonate mineral dissolution even though barite also formed (Alalli et al., 2018). With the acid spear head, the carbonate-rich shale can be more vulnerable than the clay-rich shale regarding mineral dissolution reactions.

In this study, we investigated the geochemical rock-fluid interactions during the hydraulic fracturing in HFTS-1 via experimental setup using site-specific conditions. Flow-through experiments were performed with clay-rich and carbonate-rich Wolfcamp shale cores from the HFTS project with synthetic HFF relevant to the site as part of the U.S. Department of Energy Multiscale Modeling Project (Birkholzer et al., 2021). The field cores from the HFTS project are from wells drilled through the stimulated region (Ciezobka and Reeves, 2021; Gale et al., 2018). The experiment was composed of a two-step HFF injection: with 8 min acid soaking of the reactive surface, followed by a 13-day slick water flow-through to mimic the injection method of site operators. The objective of this study is to investigate rock-fluid interactions and their impact on fluid chemistry and mineral dissolution/precipitation during the acid spear head and slick water flow-through periods. The results of this study provide insights to geochemical alterations of fluids and rocks under a field HFF injection setup, which can be useful for produced water management and scale mineral control.

## 2. EXPERIMENTAL METHODS

### 2.1 Wolfcamp Shale Cores with Milled Channels.

Two Wolfcamp shale cores from the Hydraulic Fracturing Test Sites (HFTS) in the Permian Basin were used for this study. One core is clay-rich and carbonate-poor, from 2934 m depth, with ~2360 m true vertical depth (TVD). The other core is carbonate-rich and clay-poor, from 3534 m depth, with ~2445 m TVD. The mineral composition of these cores, XRF results and selected trace elemental concentrations, analyzed and provided by our industrial collaborators, are listed in Table 1, Table S-1 and S-2.

**Table 1. Mineral composition of the Wolfcamp shale cores**

| Core ID /wt% | Quartz | Feldspar | Plagioclase | Chlorite | Illite/Smectite | Calcite | Ankerite/Dolomite | Pyrite | Organics |
|---|---|---|---|---|---|---|---|---|---|
| Clay-rich | 43 | 3 | 6 | 1 | 32 | 7 | 5 | 3 | 1 |
| Carb-rich | 17 | 2 | 5 | 1 | 11 | 34 | 27 | 2 | 0 |

The two cores were 2.54 cm in diameter and 5 cm long. They were cut in the middle to half-cylinders. For each core, one of the half cylinders cut surface was milled with two channels (~4 mm wide and ~0.5 mm deep) (Figure 1a). Both sides were polished with 400 grit (very fine) sandpaper. These channels serve as the main flow pathway so that proppants were not used to prop the fracture open. The milled channels allowed us to focus on rock-fluid interactions on the channel reactive surface and the flow pathway could remain similar in different cores for comparison.

### 2.2 Hydraulic Fracturing Fluid (HFF).

The hydraulic fracturing fluid (slick water) was prepared with synthetic diluted produced water and fracturing chemicals. The recipe was previously published (Xiong et al., 2021b). The produced water ingredients, which were based on the water chemistry provided by industrial collaborators, are listed in Table 2. The fracturing chemicals (Table 3) were modified based on a FracFocus recipe (API No.42-329-36684) used in the same region.

The hydraulic fracturing process involved two sequential injections: 1) acid-soaking for short time and 2) slick water flow-through for extended time, mimicking the field operations. After the cores were loaded in the core holders, 60 ml 15 v/v % HCl acid was injected manually through the core fracture using a syringe. All the effluent was collected, and the residual acid stayed in the cores for 8 min. The acid spearhead time was advised by site operators. Then 100 mL deionized water was flushed through the cores to rinse out the acid to minimize the damage to the flow-through experimental system. The effluent was collected in the same bottle. This mixed diluted fluid sample was considered as the acid-soaking effluent sample. Then the slick water was pumped through the cores in the flow-through system.

**Table 2. HFTS fluid ions of synthetic produced water (Xiong et al., 2021b).**

| Ions | Concentration (mg/L) |
|---|---|
| $Ca^{2+}$ | 950 |
| $Li^{+}$ | 8 |
| $Mg^{2+}$ | 200 |
| $K^{+}$ | 300 |
| $Na^{+}$ | 18500 |
| $Sr^{2+}$ | 180 |
| $HCO_3^{-}$ | 500 |
| $B(OH)_4^{-}$ | 16 |
| $Br^{-}$ | 250 |
| $Cl^{-}$ | 30750 |
| $I^{-}$ | 40 |
| $SO_4^{2-}$ | 400 |

**Table 3. HFTS fluid recipe: acid soaking and slick water (Xiong et al., 2021b).**

| Acid soaking | |
|---|---|
| 15 v/v % HCl<br>(DI water base) | Inject 60mL acid (collect the effluent), acid soaking for 8 min, inject 100mL DI water to rinse, collect the effluent in the same bottle. |
| **Slick water** | **Concentration (% mass)** |
| produced water (Table 2) | 99.512 |
| Kerosene | 0.203 |
| Methanol | 0.064 |
| Potassium metaborate | 0.019 |
| 2-Butoxyethanol | 0.031 |
| Gluteraldehyde | 0.010 |
| Guar gum | 0.007 |
| Isopropanol | 0.007 |
| Propargyl alcohol | 0.007 |
| 2-ethyl-1-hexanol | 0.007 |
| Xylene | 0.007 |
| Polyphosphonic acids | 0.007 |

| | |
|---|---|
| Potassium hydroxide | Raise pH to 9.0 before adding persulfate |
| Ammonium persulfate | 0.083 |

### 2.3 Flow-through Experimental Setup.

The flow-through experimental setup (Figure 1b) (Xiong et al., 2021a) was the same with our previous study (Xiong et al., 2021a; Xiong et al., 2020). The reservoir bottle contained the slick water to pump through the cores and it is open to the atmosphere for adequate dissolved $O_2$. The fluid was injected into each core at a relatively low rate of 0.02 mL/min to simulate the slow-flow shut-in period. The cores were placed in rubber sleeves in separate core holders. A confining pressure (13.79 MPa) was applied around the core holder via a syringe pump filled with deionized water. The core pressure (12.41 MPa) was maintained via a backpressure pump, from which the effluent samples were collected intermittently. The temperature was 66 ºC around the cores. For the experiment start-up, the fluid was injected quickly at 2 mL/min for 5 min to flush through the entire system. Then the flow rate was set to 0.02 mL/min while increasing the pressure and temperature to experimental conditions. The set-up took about 2 hrs to stabilize and the effluent from this period was removed and not analyzed. The time after the set-up period was considered as the beginning of reaction time. The Wolfcamp shale cores were originally planned to react for 3 weeks. However, leakage occurred in some connection valve in Day 13 in the flow-through system, and the experiment was stopped. Thus, the reaction time for slick water flow-through was 13 days in total. The cores were directly air dried after reaction.

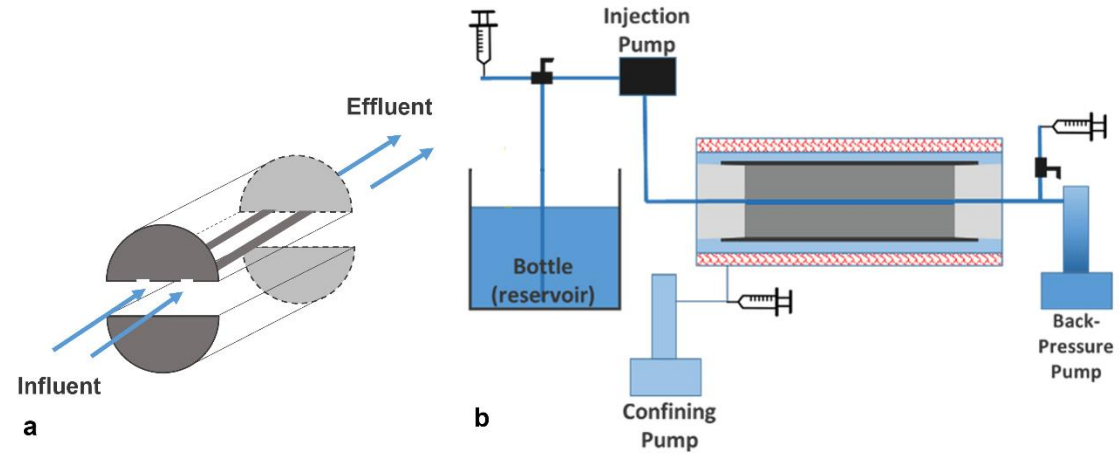


**Figure 1. a) Core milled with channels and b) flow-through experimental setup (Xiong et al., 2021a)**

### 2.4 Analytical Methods.

The concentrations in the fluid samples were measured using inductively coupled plasma mass spectrometry (ICP-MS, PerkinElmer Nexion 350D), optical emission spectrometry (ICP-OES, Perkin Elmer DV 7300) and ion chromatography (IC, DIONEX ICS-5000, Thermo SCIENTIFIC). Total dissolved inorganic carbon (DIC) and non-purgeable organic carbon (NPOC) were measured by TOC analyzer (TOC-L, SHIMADZU). Geochemists' Workbench (GWB) was used to calculate mineral saturation indices (SI) based on measured species concentrations and pH in the solution at 66 °C, using the default thermal database and the Pitzer database. The cores were scanned in-situ before and after acid soaking and flow-through reactions via X-ray computed tomography (CT, M5000 Industrial Computed Tomography System, North Star Imaging). Core surfaces were mapped using a back-scatter detector (BSE) on a scanning electron microscope (SEM, Quanta 600F, FEI) and a digital microscope (Olympus). For SEM mapping, the magnification of each slice was set at 200×. Over 1000 slices were imaged and stitched together to obtain the entire core surface. The software AZtec (Oxford Instruments) was used for SEM mapping and point analysis to compare pre- and post-reaction differences. Point analyses with energy dispersive X-Ray spectroscopy (EDS, Oxford) were performed to identify precipitation types.

The reacted cores were then cut and cross sections were made into doublet-polished microprobe-prepped thin sections (30 µm thick, prepared and scanned by Spectrum Petrographics, Inc.) for reaction front characterization (Figure 2). Regions of interest on the thin sections (red boxes on Figure 2) were analyzed via synchrotron micro-X-ray fluorescence (µ-XRF) at the Stanford Synchrotron Radiation Lightsource (SSRL, SLAC National Accelerator Laboratory, CA) beamline 7-2, with the beam conditions optimized for Fe K-edge signals. BL7-2 was equipped with a 50-µm beam size, Si(1,1,1) crystal, and four-element Si Vortex detector. The incident beam was calibrated against the iron foil at 7112eV. All maps were collected with 50 µm step size and 20 msec dwell time. Maps were collected at multiple energies of 7113, 7121.5, 7126, 7131 and 7135 eV for Fe speciation display. The selected energies are above the Fe K-edge (7112 eV) and at the absorption peaks where preliminary data showed maximum differences in normalized intensity between

the Fe K edge micro-X-ray absorption near edge structure (μ-XANES). SMAK (Sam's MicroAnalysis Kit) (Webb, 2011) was used to analyze different major components using principal component analysis (PCA). Multiple spots corresponding to different components were carefully selected for Fe XANES analysis. The XANES spectra of these spots were analyzed using Athena (Ravel and Newville, 2005) for linear combination fitting with Fe-containing end members. The number of end member Fe phases was determined by the number of distinct PCA components. The end member μ-XANES values at the corresponding multiple energies (7113, 7121.5, 7126, 7131 and 7135 eV) were put in SMAK for multiple-energy (ME) Fe map XANES fitting to obtain the end member Fe phase distribution of the areas. The method of PCA-assisted end-member XANES fitting of the ME Fe maps was described in detail in Mayhew et al (Mayhew et al., 2011) and in our previous synchrotron study (Xiong et al., 2022a). The pre-reaction Wolfcamp parent core thin sections (Figure S-1) were made and analyzed at Beamline 7-2 using the same approach with the reacted core thin sections. The pre-reaction Wolfcamp shale samples were milled to fine powders for bulk Fe K-edge XAS at Beamline 4-3.

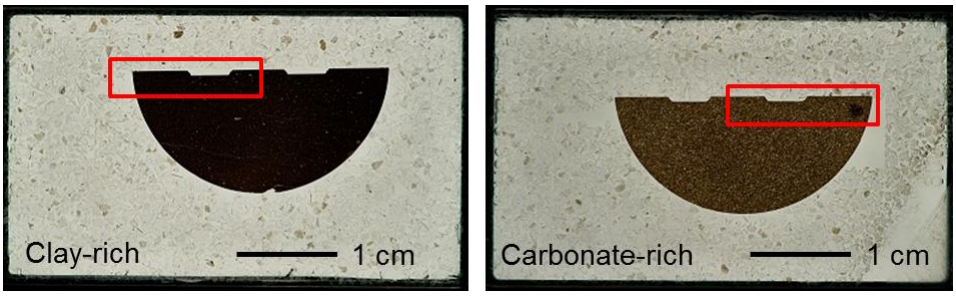


**Figure 2. Scans of the thin sections. Red boxes show the areas of the multi-energy XRF maps.**

### 2.5 Reactive Transport Modeling.

Reactive transport modeling was performed to examine alteration caused by acid soaking and slick water injection, and to compare the impacts of initial mineralogy (i.e., carbonate rich vs. clay rich). The simulations were performed using the coupled CrunchTope-COMSOL framework, which has been described in detail and applied to investigate mineral interface alteration in previous studies (Deng et al., 2022; Deng et al., 2021)

In this study, the computational domain was a 2D cross section along the core, capturing half of the channel (0.25 mm) and half of the core matrix under the assumption of symmetry. The mineral compositions for the carbonate rich and clay rich simulations follow the compositions reported in Table 1, and the influents had chemical compositions from the ICP and IC measurements of the experimental influent samples. An initial matrix porosity of 3% was assumed for all simulations.

The domain was initially filled with strong acid for ~8 min, and then flushed out with DI water. Afterwards, the slick water was injected at an average velocity of 5 mm/min for 13 days as in the experiments. The reaction networks and rate constants are the same as those used in our previous study (Xiong et al., 2021a).

## 3. RESULTS AND DISCUSSION

### 3.1 Fluid Chemistry.

#### *3.1.1 Acid Soaking Fluid.*

The species concentrations in the acid soaking samples were shown in Figure 3. The carbonate-rich shale released much more Ca, Mg, Fe, and inorganic carbon during the acid soaking than the clay-rich shale, indicating intense carbonate mineral dissolution during acid exposure. Although the clay-rich shale contained slightly more pyrite (3 wt%) than the carbonate-rich shale (2%) (Table 1), the released sulfate from clay-rich shale was significantly lower compared to that from the carbonate-rich shale (Figure 3). The pyrite is the main S source in these cores during acid soaking. In the carbonate-rich shale, the calcite dissolution led to physical detachment of embedded pyrite (Kreisserman and Emmanuel, 2018), leading to more pyrite exposing to the acid for oxidative dissolution than the clay-rich shale. Some minor species including Cr, P, Ba, Ni, Cu, etc. were released from the shale during acid exposure.

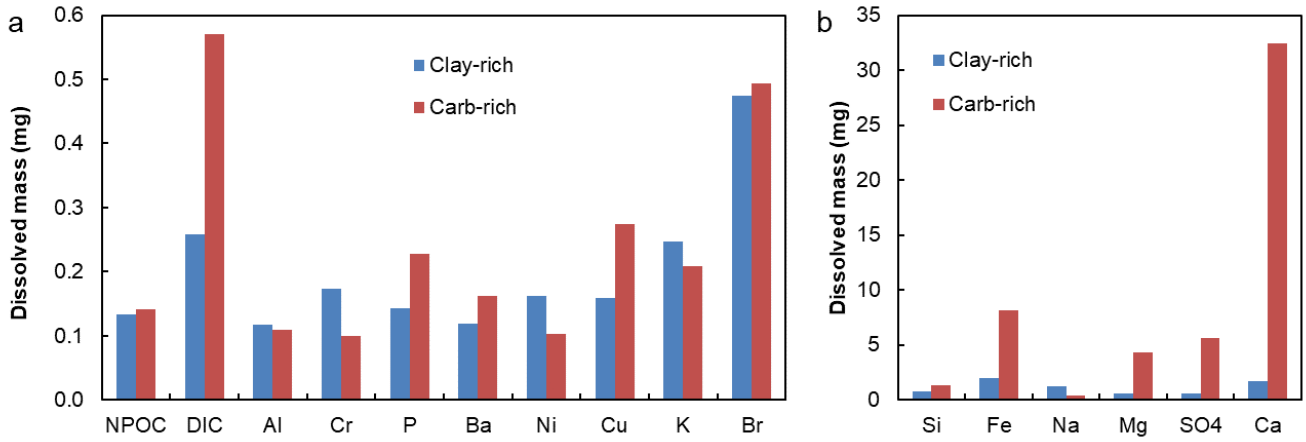


**Figure 3. Dissolved ion masses from acid-soaking based on fluid sample analysis. NPOC is non-purgeable organic carbon. DIC is total dissolved inorganic carbon.**

### *3.1.2 Flow-through Fluid.*

The Ca concentrations in the effluent from both shale cores were similar to that in the influent, indicating limited calcite dissolution (Figure 4d). After the acid-soaking treatment, the slick water for the flow-through injection had a near-neutral pH (Figure 4h). The similarity of Ca concentrations in the effluent and the influent may be due to fewer calcite minerals in the reaction front and/or less dissolution in much higher pH. Carbonate-rich core released more Fe, Ba and Cr (Figure 4b, 4e, 4f). Clay-rich core released more $SiO_2$(aq) and phosphate (Figure 4c, 4g). Pyrite dissolution continued to happen during the slick water flow-through, indicated by the increased sulfate (Figure 4a) and Fe concentrations in the effluent samples of both cores. However, the concentration differences between the effluent and the influent did not match stoichiometrically with pyrite ($FeS_2$) dissolution, with $\Delta S$ ~250 mg/L and $\Delta Fe$ ~5 mg/L and ~15 mg/L, respectively, for the clay-rich and carbonate-rich shale. Pyrite oxidative dissolution can be summarized in the following reactions:

$$FeS_2 + 3.5O_2 + H_2O \rightarrow Fe^{2+} + 2SO_4^{2-} + 2H^+ \quad (1)$$

The dissolved $Fe^{2+}$ can be further oxidized to $Fe^{3+}$ and form precipitates such as $Fe(OH)_3$:

$$Fe^{2+} + 0.25O_2 + H^+ \rightarrow Fe^{3+} + 0.5H_2O \quad (2)$$

$$Fe^{3+} + 3H_2O \rightarrow Fe(OH)_3 + 3H^+ \quad (3)$$

The excessive sulfate concentration came from the thermal decomposition of ammonium persulfate, which was added as a breaker in the HFF. At the experimental temperature (66 ºC), persulfate could be easily decomposed to sulfate and $SO_4^{-\cdot}$ radical oxidant (Manz and Carter, 2017), which facilitated Fe(II) oxidation in addition to dissolved $O_2$. Fe oxidation rate is much faster at near neutral pH compared with acidic pH (Morgan and Lahav, 2007; Palandri and Kharaka, 2004). The small aqueous Fe concentration in the effluent (Figure 4b) may be the residual Fe after Fe(II) oxidation and Fe(III) precipitation (which was observed and discussed below) in the oxidative environment at near neutral pH. The pH in both the effluent samples decreased to ~6 as a result of pyrite dissolution (Figure 4g).

The mineral dissolution was not significant during the slick water flow-through period, probably due to the near-neutral pH. The clay-rich shale saw slightly larger aqueous Si concentration in the effluent than the carbonate-rich shale, indicating more silicate clay dissolution. Other minor species increased in the effluent include Ba, Cr, and phosphate, which are related to the mineral precipitations observed and discussed below. During the flow-through period, the dissolved inorganic carbon concentrations in both effluent samples decreased (Figure 5a) comparing with the influent DIC. The decreased inorganic carbon in the effluent compared to the influent indicated some carbonate mineral precipitation. While during the acid soaking, carbonate mineral dissolution is predominant and DIC was released in the acid soaking effluent (Figure 3a) in both cores. The non-purgeable organic carbon concentration is shown in Figure 5b.

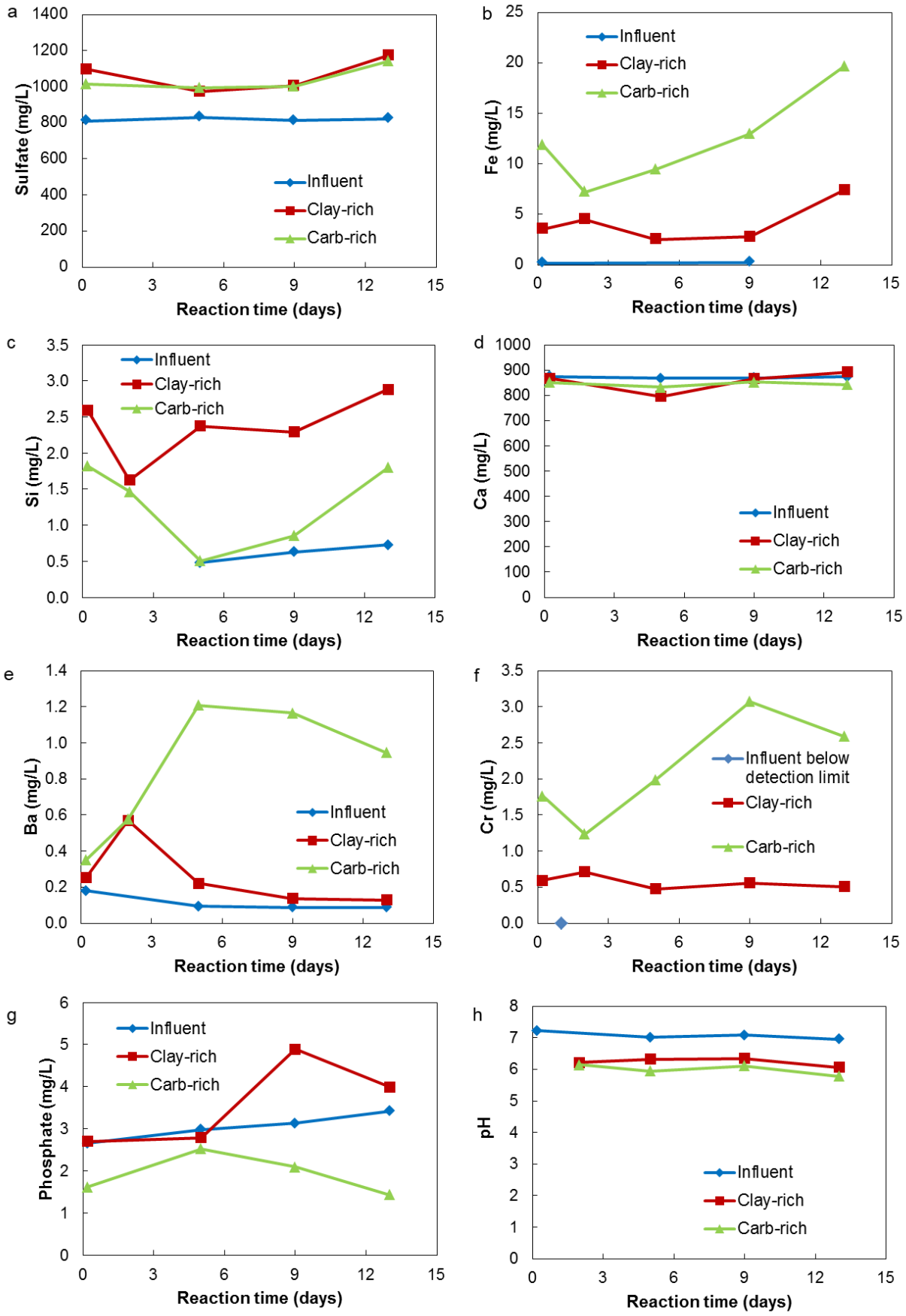


**Figure 4. Selected aqueous species concentrations and pH in the influent and effluent. Blue line is influent. Red and Green lines are effluent.**

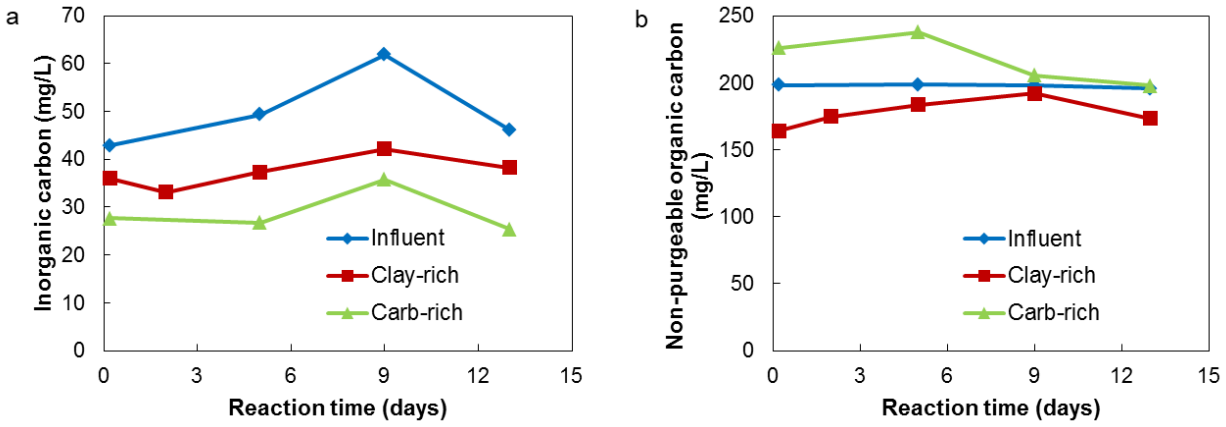


**Figure 5. Dissolved inorganic carbon and non-purgeable organic carbon in the influent and effluent. Blue line is influent. Red and Green lines are effluent.**

### *3.1.3 Mineral Saturation Indices.*

Saturation indices of minerals in the influent and Day 5 effluent samples were listed in Table 4. The full aqueous chemistry data used for calculation in GWB is listed in Table S-3. The default thermal database included much more species, especially for carbon and silica related species, however, it may not be accurate for solutions with high total dissolved solids (TDS). The Pitzer database is suitable for high TDS solutions but lacks C and Si related species. Calculating SI using both database could provide supplementary information. Table 4 lists SI results calculated using Pitzer database and the default database.

If the SI is above 0, it means the mineral has the tendency to precipitate from the fluid. However, it may not actually precipitate in real reactions if the mineral has a high nucleation energy barrier. Several chromate minerals and Ca-phosphate minerals are supersaturated. Multiple carbonate minerals were slightly supersaturated in the influent and the SI decreased significantly in the effluent samples, indicating the formation of carbonate minerals. However, no obvious carbonate minerals were found in the surface characterization, which is not surprising. Because 1) the SI calculation regarding the carbonate minerals uses the default database, which may not be accurate for high TDS solutions 2) carbonate minerals require relatively high SI to overcome the energy barrier to nucleate and precipitate in real situation. The slick water flow-through effluents show similar chemistry and saturation indices for both the clay-rich and carb-rich cores. The acid soaking resulted in very different effluent chemistry for the clay-rich and carb-rich cores. This indicates that the acid soaking step impacts the type of core (especially carbonate-rich cores) more significantly than the slick water flow-through step.

**Table 4. Calculated mineral saturation indices on Day 5 influent and effluent samples.**

| Pitzer database - Day 5 samples | | | | Thermo (default) database - Day 5 samples | | | |
|---|---|---|---|---|---|---|---|
| SI=log Q/K | Influent | Clay-rich | Carb-rich | SI=log Q/K | Influent | Clay-rich | Carb-rich |
| $ZnCr_2O_4$ | | 30.13 | 27.21 | $ZnCr_2O_4$ | | 23.33 | 21.35 |
| $FeCr_2O_4$ | | 23.35 | 22.15 | $FeCr_2O_4$ | | 16.87 | 16.62 |
| $Cr_2O_3$ | | 21.81 | 20.79 | $Cr_2O_3$ | | 15.79 | 15.71 |
| $MgCr_2O_4$ | | 19.55 | 17.76 | $CuCr_2O_4$ | | 14.16 | 13.8 |
| $CuFeO_2$(c) | | 11.5 | 10.82 | $MgCr_2O_4$ | | 13.55 | 12.72 |
| Hydroxyapatite | 14.13 | 11.24 | 9.648 | $CuFeO_2$(c) | | 10.36 | 9.912 |
| Whitlockite | 7.544 | 6.083 | 5.267 | Hydroxyapatite | 10.51 | 7.531 | 5.783 |
| Celestite | 0.1187 | 0.1701 | 0.1896 | Whitlockite | 5.182 | 3.663 | 2.739 |
| Tenorite | 0.04752 | -0.1368 | -0.6419 | Strontianite | 1.997 | 1.023 | 0.3654 |
| | | | | Dolomite | 1.966 | 0.05999 | -1.297 |

| | | | | |
|---|---|---|---|---|
| | $Co_2SiO_4$ | 1.583 | 1.031 | -1.049 |
| | Calcite | 0.6191 | -0.3491 | -1.014 |
| | Aragonite | 0.458 | -0.5101 | -1.175 |
| | Celestite | -0.0811 | -0.0212 | 0.0017 |

### 3.2 Core Characterization.

#### *3.2.1 Mineral Dissolution and Precipitation on Reactive Surface.*

The entire cut surfaces of the cores were mapped in SEM and using a digital microscope (Figure 6). For the clay-rich shale core, a lot of orange Fe (hydro)oxides precipitates were found on the reactive surfaces, especially at the region of the flow inlet (bottom of the core). These Fe (hydro)oxides were not found in large scale in microscopic images in the carbonate-rich shale core surface, although the carbonate-rich shale contains relatively higher Fe contents than the clay-rich shale before reaction (Table S-1). Some of the Fe (hydro)oxides precipitates may come from the release of Fe from the shale, which was indicated by the fluid chemistry. A previous study also showed that the Fe released from steel and Fe complexation/precipitates formed during steel-HFF interactions could be carried over with the fluid and settled on the shale surface (Xiong et al., 2022b). For the carbonate-rich shale core, the color of the flow pathways was visibly lighter than the unreacted surface (Figure 6), indicating mineral dissolution and leaching at the reactive surface. The lighter color reactive surface may be primarily formed during the acid soaking. Based on results in previous section 3.1, the mineral dissolution mainly occurred during the acid soaking step, whereas the secondary minerals precipitated during the slick water flow-through period.

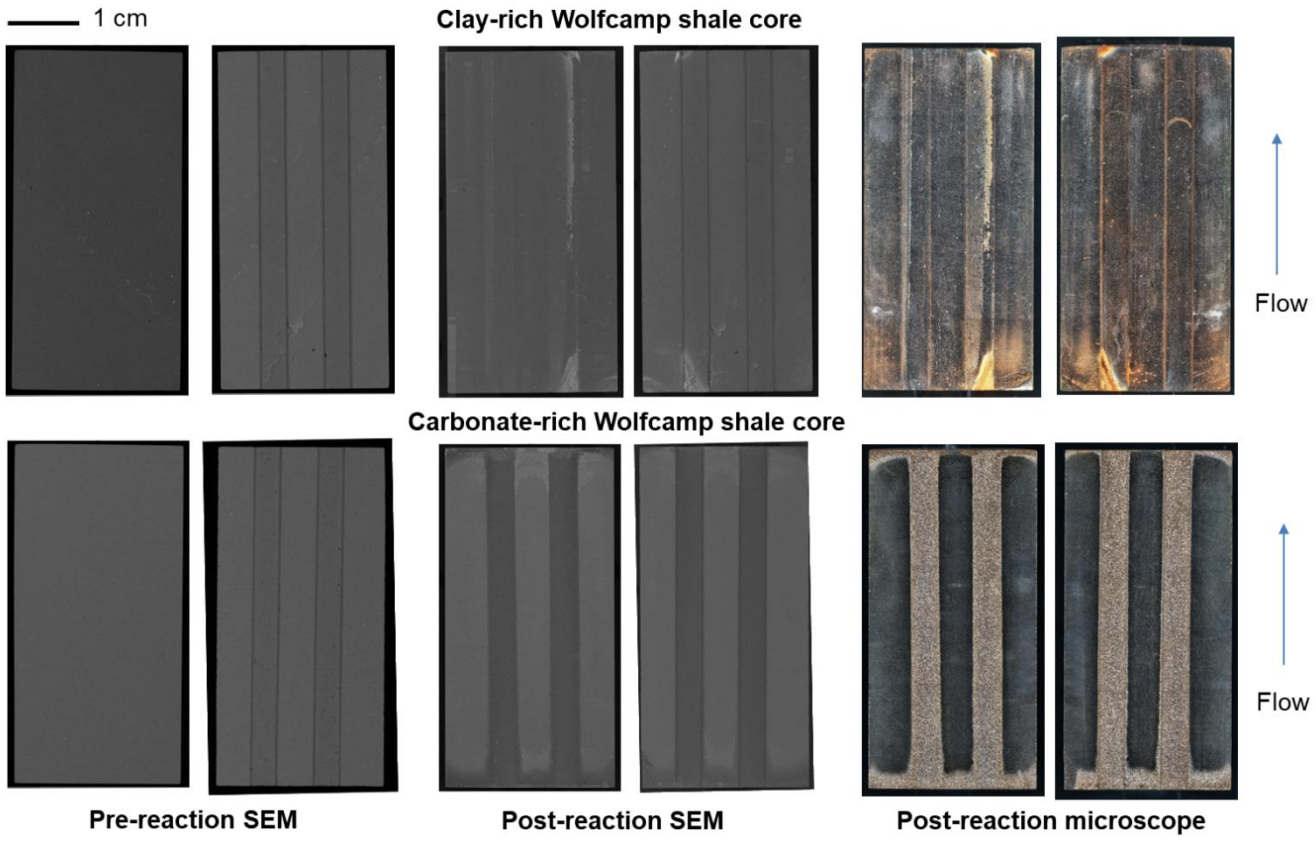


**Figure 6. Core surface images before and after reaction. The flow direction is from bottom to top for all samples.**

Mineral precipitations were closely examined by comparing the pre- and post-reaction high resolution SEM mapping. Limited secondary precipitates were observed and identified on the reacted channel surfaces (Figure 7, 8). The mineral precipitate types were similar in both shale cores. In clay-rich cores, precipitate mixtures including Fe (hydro)oxides/chromates and Ca-phosphate were found (Figure 7a, 7b), which is consistent with the SI calculations (Table 4) based on the fluid chemistry. There are also pure clusters of round Fe (hydro)oxides particles (Figure 7c). A few sulfate minerals, such as anhydrite, celestite and barite were found on the reactive surface in the clay-rich core (Figure 7d, 7e). In the carbonate-rich core, similar mixture of Fe (hydro)oxides/chromates and Ca-phosphate were

found (Figure 8a). Limited barite precipitates were observed in the carbonate-rich core (Figure 8b). Since the synthetic HFF did not contain any Ba, the Ba in the barite came from the shale (Table 3). Ba can be released during hydraulic fracturing process in high ionic strength conditions (Renock et al., 2016). Some pyrite on the surface was found to be oxidized (Figure 8c). However, it was difficult to determine if the oxidation was through the experiment reactions or pre-existing, because the synchrotron analysis discussed below showed certain amount of Fe(III) in both pre-reaction shale cores. On the reacted surface of both cores, obvious acid etching spots were observed (Figure 7,8).

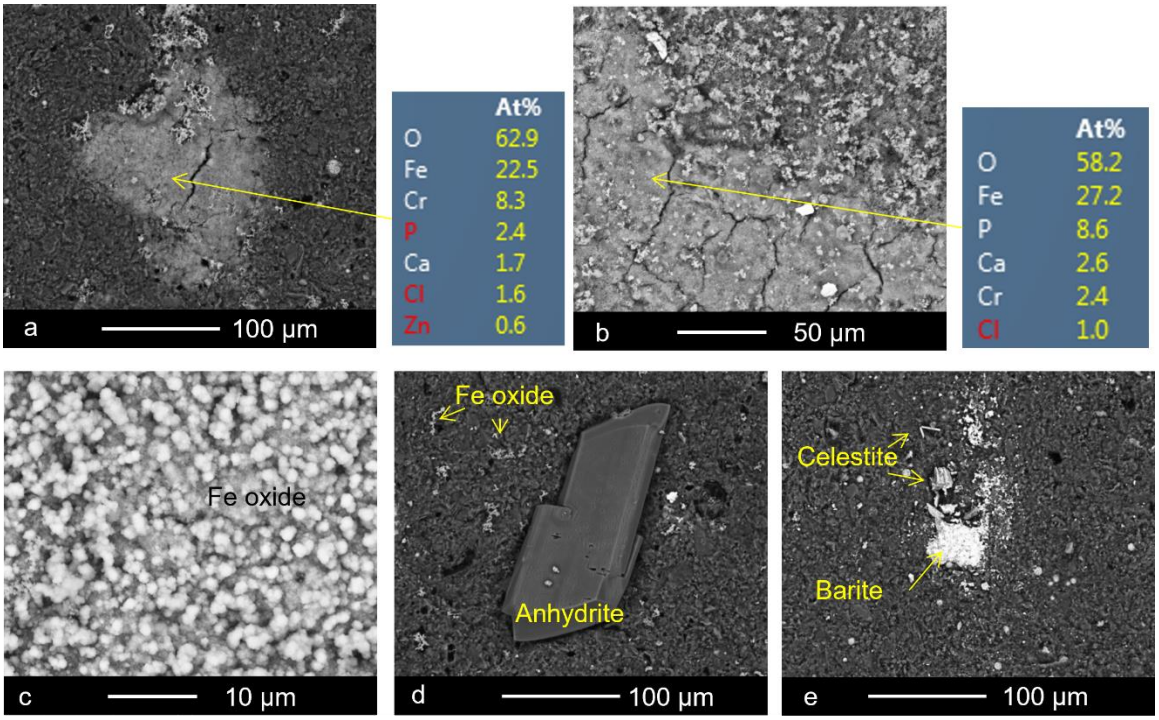


**Figure 7. SEM images of secondary precipitates on the reacted clay-rich core.**

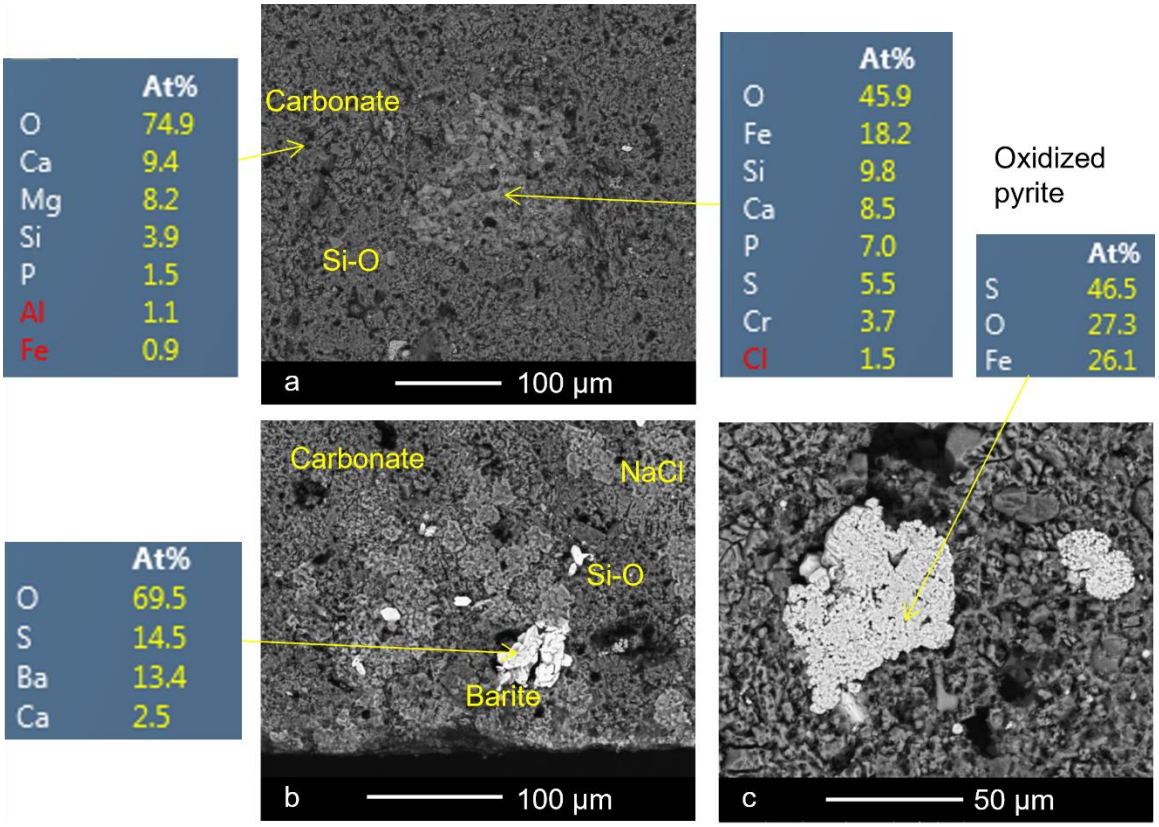


**Figure 8. SEM images of the surface of the reacted carbonate-rich core.**

***3.2.2 Reaction Front via Synchrotron analysis.***

The PCA analysis of the ME maps showed three distinct components for both shales (Figure S-2), indicating that three Fe major end members are present in the shale. Multiple different spots were selected based on the component maps for Fe micro-XANES analysis (spot locations on Figure S-2). The μ-XANES spectra were fitted by cycle-fitting with a series of Fe-containing minerals described in the previous study (Xiong et al., 2022a). One of the end members was pyrite (Table 1). Ferrihydrite was chosen to represent newly-formed secondary Fe(III) precipitates. The third end member displayed two distinct peaks at 7125.7 eV and 7134.4 eV (black dashed lines in Figure 9), which did not match well with any of our mineral standards, nor common Fe-containing mineral XANES in the publications. The third end member was also present in the spot XANES of both pre-reaction shale thin sections. The spot locations and XANES of this end member are shown in Figure 9 with the fitted end-member distribution maps for better illustration, instead of the component maps. This third end member has a XANES edge (E0) at 7123.4 eV (similar with ferrihydrite E0 at 7122.8 eV), meaning it is predominantly Fe(III). We name this end member "Fe(III)*" here and below. Since Fe(III)* appeared in both the pre-reaction and post-reaction shale samples with its distinct peaks, the spot XANES of Fe(III)* was chosen as the third end member standard (the spot XANES of the carbonate-rich shale in Figure 9). For each XRF map, several hot spots based on PCA analysis were chosen for XANES analysis to check the fitting goodness of the three chosen end-members (pyrite, ferrihydrite and Fe(III)*). Some spot XANES fitting examples were shown in Figure S-3, with comparison to the end-members XANES. The full list of spot XANES analysis of the post-reaction thin sections were listed in Table S-4. These end-members are suitable to represent Fe phases in the sample.

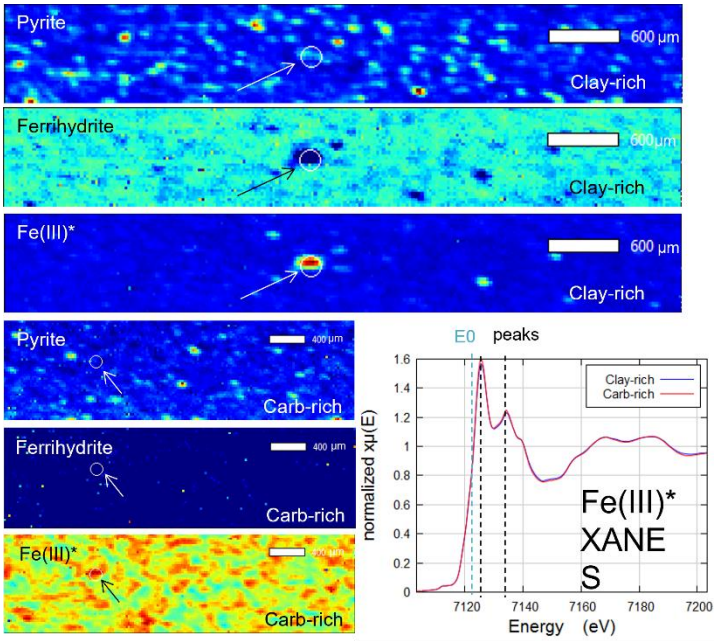


**Figure 9. Processed Fe end-member distribution maps of the pre-reaction clay-rich and carbonate-rich thin section shale samples, with one example XANES spot on each sample showing the Fe(III)* phase. The color scale of photon intensity was set to default range for each end-member maps to emphasize Fe(III)* hot spots.**

Figure 10 shows the bulk XANES analysis on the pre-reaction shale powders. Both the clay-rich and the carbonate-rich Wolfcamp shale samples already contained a lot of pre-existing Fe(III) before the experimental reaction. The clay-rich shale contained about 47.3% Fe(II) as pyrite, 40.8% Fe(III) as ferrihydrite, and 11.9% Fe(III)*. The carbonate-rich shale contained about 16.2% pyrite and 83.8% Fe(III)*. From the SEM-EDX analysis, the pyrite grains in the carbonate-rich shale mostly contained appreciable amount of O (Figure 8). The Fe(III)* phase may include a small part of the partially oxidized pyrite. However, the lack of correlation between Fe(III)*, pyrite and ferrihydrite from the XRF maps (Figure 9) indicate that Fe(III)* was a distinctive phase, different from known Fe(III) species in our available database. The Fe(III)* map had good correlation with Ca and P XRF maps (Figure S-4). But the vivianite mineral standard with Fe(II) did not fit the XANES of Fe(III)*.

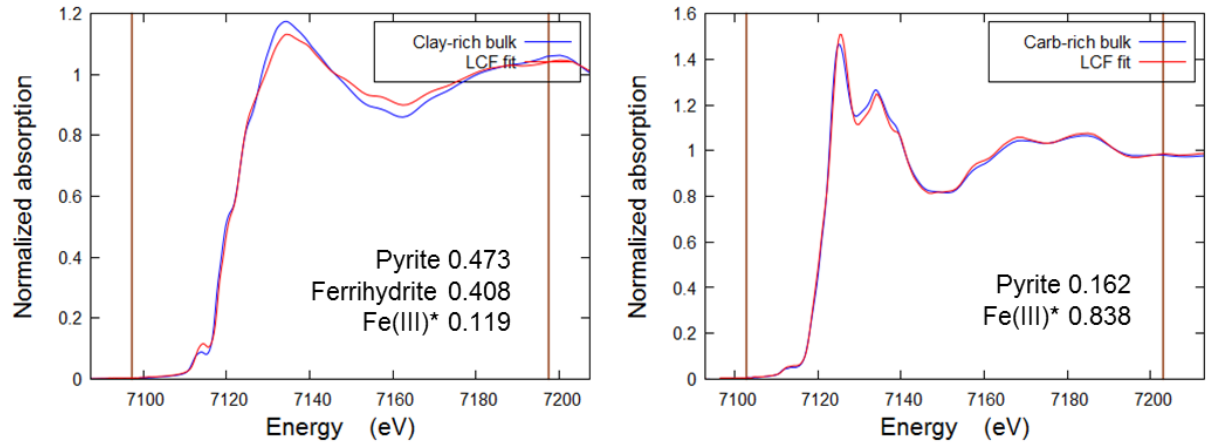


**Figure 10. Bulk analysis of XANES on the pre-reaction shale powders.**

The fitted Fe distribution maps present as in pyrite, ferrihydrite and Fe(III)* end members are shown in Figure 11 together with elemental XRF maps of Ca and P for comparison. Ca and P signals may over overlap as shown in Figure 11, due to P K line signal (2keV) overlap with potential escape peak (2keV) from Ca K line signal (4keV). But this overlap does not impact our result discussion. The ferrihydrite in both shale thin sections are present as an accumulated thin layer of 10~50 µm at the shale-HFF interface. The accumulated thin ferrihydrite layer seems to be the newly formed Fe(III)-containing precipitates apart from the pre-existing Fe(III) phases. The new ferrihydrite layer as a result of rock-fluid interactions was limited to the narrow layer near the shale surface. Fe(III)* aligned with the Ca and P distribution as observed in the pre-reaction thin section analysis, yet we did not find a Fe(III) mineral standard containing Ca and P to fit this phase.

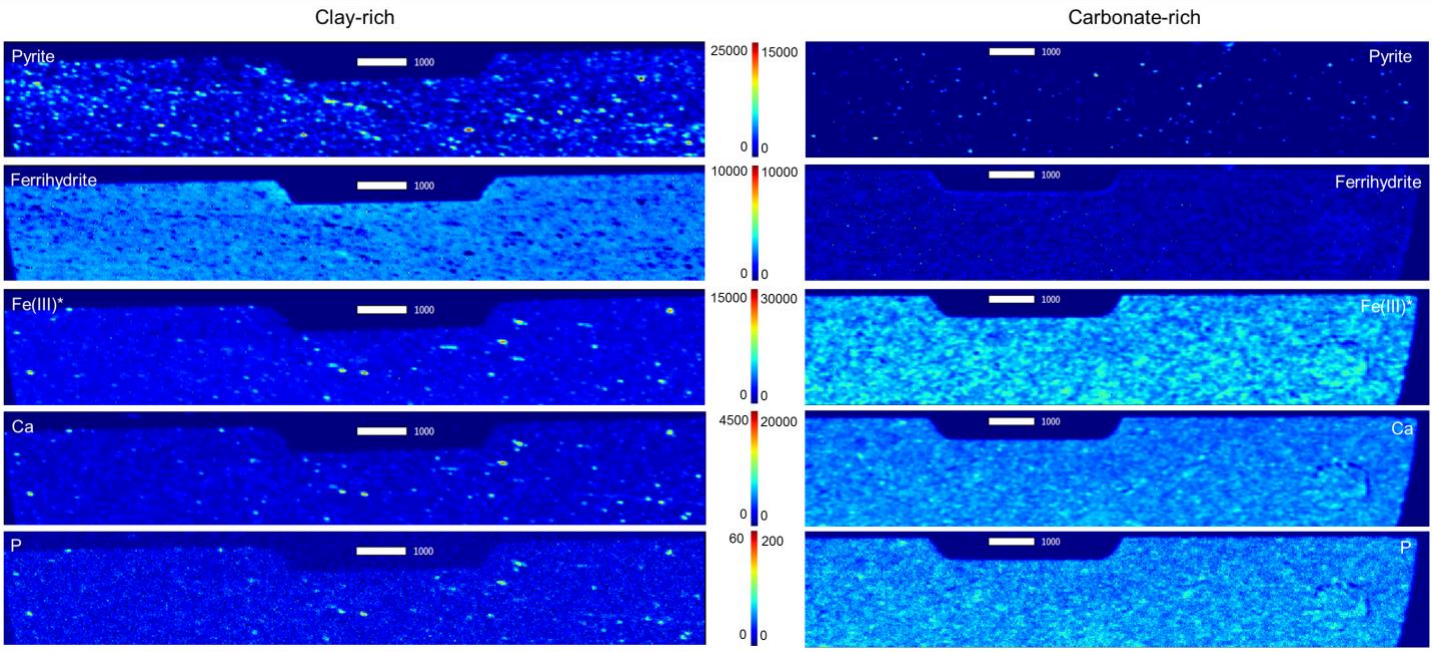


**Figure 11. Fe end member distribution maps (pyrite, ferrihydrite and Fe(III)*) and XRF maps of Ca and P for the reacted shale core thin-sections (scale bar is 1000 μm).**

For the carbonate-rich shale, the Ca intensity near the reactive surface was slightly lower than that in the deeper shale matrix region (Figure 12), indicating some extent of Ca leaching from the shale matrix to the fluid during reaction, although the Ca leaching region was not obviously defined in the map. For the clay-rich shale, the average intensity along the x-axis is ten times lower than that in the carb-rich shale. The limited amount of carbonate mineral grains are scattered in the shale matrix. It is difficult to tell if the near-interface region has Ca leaching layer.

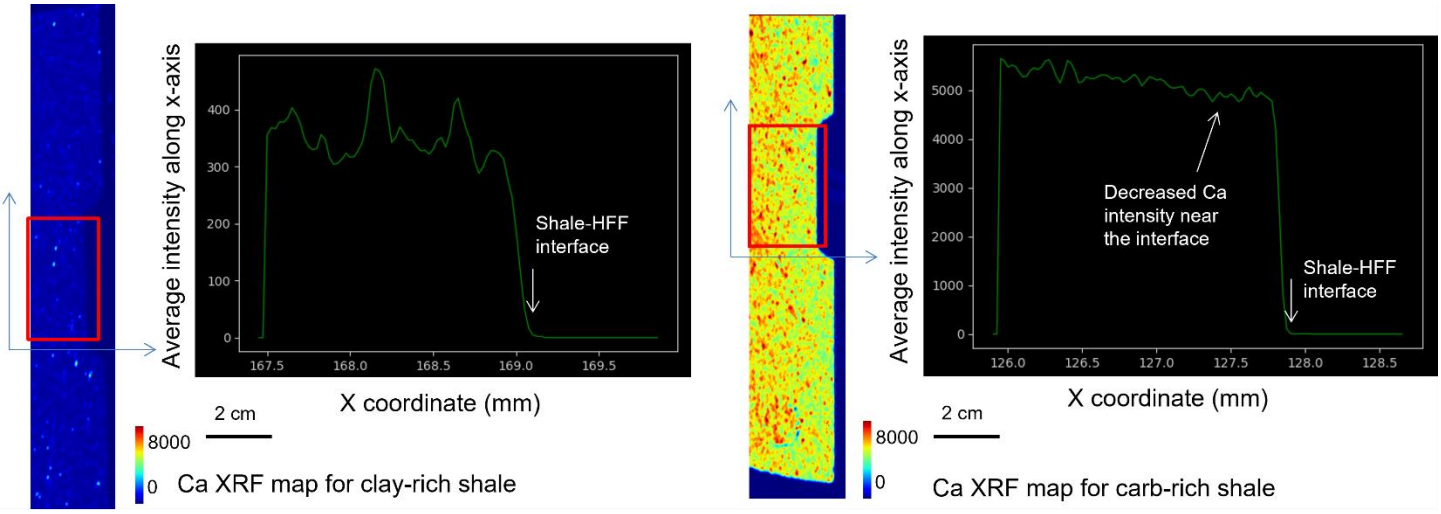


**Figure 12. Ca XRF average intensity along the x-axis to show the Ca leaching near the shale-HFF interface in the clay-rich and carbonate-rich shale thin sections. Red boxes mark the area selected for average intensity calculation.**

### 3.3 Reactive Transport Modeling.

Figure 13 shows the results of reactive transport modeling, highlighting the geochemical gradients close to the inlet from the center of the fracture to the rock matrix. The rock-fluid interface is at 0.25 mm, as the channel aperture is 0.5 mm. As shown in Figure 13(a), after the initial acid soaking, the pH in the fracture is the same as the influent and the pH increases gradually moving into the matrix. After the flushing of DI water, the pH in the fracture increases, but there is a zone with relatively low pH at the interface between the fracture and matrix, as the fluid in the matrix is not flushed and the pH change is dominated by diffusion. After 13 days of reaction, the pH in the interface zone increases because of calcite dissolution. The pH increase is slightly smaller in the clay rich sample than the carbonate rich sample, because of a smaller amount of calcite available for buffering the pH (Figure 13(b)). For the same reason, the calcite dissolution front goes deeper into the matrix in the clay rich sample (Figure 13(b)). In the simulations of both samples, precipitation of ferrihydrite was predicted at the fracture-matrix interface zone. The amount of precipitation in the clay rich sample is

about one order of magnitude higher than that in the carbonate rich sample, which is likely attributed to the slow dissolution of Fe-bearing clay minerals.

The reaction front indicated by the model is consistent with the experimental results. The pH profile shows a reaction front about 1 mm from the interface into the matrix. This matches well with the 1~2 mm Ca-leaching zone in the carbonate-rich shale core (Figure 12). The dissolution reaction front seems to be determined during acid spearhead and the slick water flow-through does not penetrate further into the matrix.

During the sequential injections, the Ca leaching near the rock-fluid interface was primarily a result of the acid soaking step, as mineral dissolution was much more intense during acid exposure than during the slick water flow-through period. A previous modeling study showed acid spearhead is a crucial factor to determine the spatial distribution of reactions in a sequential injection protocol in the flow-through system (Li et al., 2022).

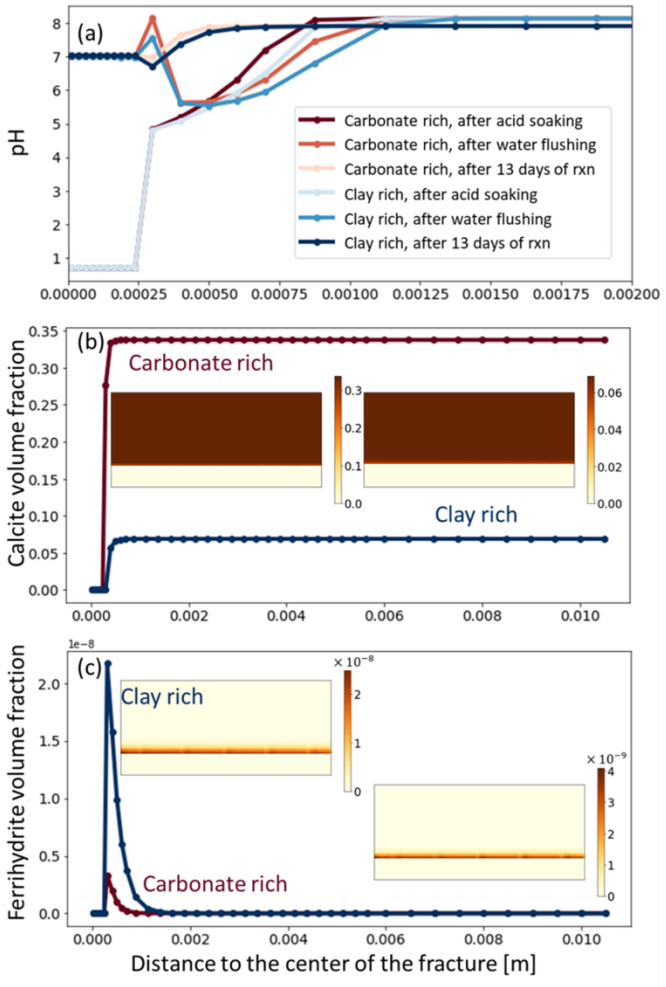


**Figure 13. Vertical profiles at 1cm from the inlet cross-cutting the fracture and matrix for (a) pH, (b) calcite volume fraction, and (c) ferrihydrite volume fraction. The x-axis is the distance between the fracture center and the matrix, and 0.25 mm is the rock-fluid interface. The insets in (b) and (c) are colormaps of the entire 2D computational domain at the end of experiment time, i.e., 13 days, where the bottom is the fracture center.**

## 4. CONCLUSIONS

During hydraulic fracturing field operations in Permian Basin, acid spearhead is an important step to dissolve minerals close to the shale surface and create reaction front for fluid access into deeper matrix. Calcite dissolution is the primary geochemical reaction during the acid spearhead period to create pathways for HFF penetration, especially for the carbonate-rich shale. For the clay-rich shale, the dissolution layer is not obvious at the rock-fluid interface. This results in significant more dissolved inorganic carbon and calcium in the acid leaching from the carbonate-rich shale than that from the clay-rich shale. The subsequent slick water with almost neutral pH provides a favored environment for Fe oxides to precipitate. A thin layer of ferrihydrite was observed on the rock-fluid interface in both clay-rich and carb-rich cores. The finding of the unidentified Fe(III)* phase has not been reported previously for Wolfcamp shale at HFTS-1. This phase is generally present in the shale even before the experiment. More studies may be needed in the future on this

original oxidized Fe phase. Overall, limited scaling minerals formed during the reaction. The precipitates on the rock-fluid interface are less likely to cause problems to gas and oil transport pathways. These findings provide insight to the geochemical interactions and their impacts during hydraulic fracturing injection in the Permian Basin.

## ASSOCIATED CONTENT

Supporting information: Chemistry of the shale; Pre-reaction cores thin section scans; Principle component analysis maps with spot locations for XANES; Spot XANES linear combination fitting analysis; Example of spot XANES analysis with pyrite, ferrihydrite and Fe(III)* XANES; Ca and P XRF maps and the Fe(III)* distribution map, and the correlation analysis of Fe(III)* and Ca; Spot XANES Linear Combination Fitting analysis.

## ACKNOWLEDGMENTS

This work was performed in support of the U.S. Department of Energy's Fossil Energy and Carbon Management's Office of Oil & Gas and executed through the National Energy Technology Laboratory (NETL) Research & Innovation Center's Onshore Unconventional Resources FWP. Use of the Stanford Synchrotron Radiation Lightsource, SLAC National Accelerator Laboratory, is supported by the U.S. Department of Energy, Office of Science, Office of Basic Energy Sciences. Thanks to GTI Energy for providing the Wolfcamp shale cores. Many thanks to the people who assisted synchrotron data collection: Sharon Bone, Erik Nelson, and Sam Webb. We thank the technical team who conducted the X-ray CT scan and the flow-through experiment at NETL Morgantown and the analysts at NETL Pittsburgh Analytical Laboratory.

## DISCLAIMER



## REFERENCES

Alalli, A., Li, Q., Jew, A., Kohli, A., Bargar, J., Zoback, M., Kovscek, A., 2018. Effects of hydraulic fracturing fluid chemistry on shale matrix permeability, SPE/AAPG/SEG Unconventional Resources Technology Conference. URTEC, p. D013S015R009.

Balaba, R.S., Smart, R.B., 2012. Total arsenic and selenium analysis in Marcellus shale, high-salinity water, and hydrofracture flowback wastewater. Chemosphere 89, 1437-1442.

Birkholzer, J.T., Morris, J., Bargar, J.R., Brondolo, F., Cihan, A., Crandall, D., Deng, H., Fan, W., Fu, W., Fu, P., Hakala, A., Hao, Y., Huang, J., Jew, A.D., Kneafsey, T., Li, Z., Lopano, C., Moore, J., Moridis, G., Nakagawa, S., Noël, V., Reagan, M., Sherman, C.S., Settgast, R., Steefel, C., Voltolini, M., Xiong, W., Ciezobka, J., 2021. A New Modeling Framework for Multi-Scale Simulation of Hydraulic Fracturing and Production from Unconventional Reservoirs. Energies 14, 641.

Chen, H., Carter, K.E., 2017. Characterization of the chemicals used in hydraulic fracturing fluids for wells located in the Marcellus Shale Play. J Environ Manage 200, 312-324.

Ciezobka, J., Courtier, J., Wicker, J., 2018. Hydraulic fracturing test site (HFTS)–project overview and summary of results, Unconventional Resources Technology Conference, Houston, Texas, 23-25 July 2018. Society of Exploration Geophysicists, American Association of Petroleum …, pp. 1331-1339.

Ciezobka, J., Reeves, S., 2021. Overview of Hydraulic Fracturing Test Sites (HFTS) in the Permian Basin and Summary of Selected Results (HFTS-I in Midland and HFTS-II in Delaware), Latin America Unconventional Resources Technology Conference, 16-18 November 2020. Unconventional Resources Technology Conference (URTEC), pp. 93-102.

Deng, H., Poonoosamy, J., Molins, S., 2022. A reactive transport modeling perspective on the dynamics of interface-coupled dissolution-precipitation. Applied Geochemistry 137, 105207.

Deng, H., Tournassat, C., Molins, S., Claret, F., Steefel, C., 2021. A Pore-Scale Investigation of Mineral Precipitation Driven Diffusivity Change at the Column-Scale. Water Resour Res 57, e2020WR028483.

Field, C.B., Barros, V.R., Mach, K.J., Mastrandrea, M.D., Aalst, M., Adger, W.N., Arent, D.J., Barnett, J., Betts, R., Bilir, T.E., Birkmann, J., Carmin, J., Chadee, D.D., Challinor, A.J., Chatterjee, M., Cramer, W., Davidson, D.J., Estrada, Y.O., Gattuso, J.P., Hijioka,

Y., Hoegh-Guldberg, O., Huang, H.Q., Insarov, G.E., Jones, R.N., Kovats, R.S., Lankao, P.R., Larsen, J.N., Losada, I.J., Marengo, J.A., McLean, R.F., Mearns, L.O., Mechler, R., Morton, J.F., Niang, I., Oki, T., Olwoch, J.M., Opondo, M., Poloczanska, E.S., PÃ¶rtner, H.O., Redsteer, M.H., Reisinger, A., Revi, A., Schmidt, D.N., Shaw, M.R., Solecki, W., Stone, D.A., Stone, J.M.R., Strzepek, K.M., Suarez, A.G., Tschakert, P., Valentini, R., VicuÃ±a, S., Villamizar, A., Vincent, K.E., Warren, R., White, L.L., Wilbanks, T.J., Wong, P.P., Yohe, G.W., 2014. Technical Summary, in: Field, C.B., Barros, V.R., Dokken, D.J., Mach, K.J., Mastrandrea, M.D., Bilir, T.E., Chatterjee, M., Ebi, K.L., Estrada, Y.O., Genova, R.C., Girma, B., Kissel, E.S., Levy, A.N., MacCracken, S., Mastrandrea, P.R., White, L.L. (Eds.). Cambridge University Press, Cambridge, United Kingdom and New York, NY, USA.

Flynn, S.L., von Gunten, K., Warchola, T., Snihur, K., Forbes, T.Z., Goss, G.G., Gingras, M.K., Konhauser, K.O., Alessi, D.S., 2019. Characterization and implications of solids associated with hydraulic fracturing flowback and produced water from the Duvernay Formation, Alberta, Canada. Environ Sci Process Impacts 21, 242-255.

Gale, J.F., Elliott, S.J., Laubach, S.E., 2018. Hydraulic fractures in core from stimulated reservoirs: core fracture description of HFTS slant core, Midland Basin, West Texas, Unconventional Resources Technology Conference, Houston, Texas, 23-25 July 2018. Society of Exploration Geophysicists, American Association of Petroleum …, pp. 1340-1357.

Haluszczak, L.O., Rose, A.W., Kump, L.R., 2013. Geochemical evaluation of flowback brine from Marcellus gas wells in Pennsylvania, USA. Applied Geochemistry 28, 55-61.

Harrison, A.L., Jew, A.D., Dustin, M.K., Thomas, D.L., Joe-Wong, C.M., Bargar, J.R., Johnson, N., Brown, G.E., Maher, K., 2017. Element release and reaction-induced porosity alteration during shale-hydraulic fracturing fluid interactions. Applied Geochemistry 82, 47-62.

Jew, A.D., Brownlow, J.W., 2025. Inorganic Alterations in Unconventional Shale Reservoirs: Importance of Additive and Base Fluid Chemistry. Energy & Fuels.

Jew, A.D., Dustin, M.K., Harrison, A.L., Joe-Wong, C.M., Thomas, D.L., Maher, K., Brown, G.E., Bargar, J.R., 2017. Impact of Organics and Carbonates on the Oxidation and Precipitation of Iron during Hydraulic Fracturing of Shale. Energy & Fuels 31, 3643-3658.

Khan, H.J., Spielman-Sun, E., Jew, A.D., Bargar, J., Kovscek, A., Druhan, J.L., 2021. A Critical Review of the Physicochemical Impacts of Water Chemistry on Shale in Hydraulic Fracturing Systems. Environ Sci Technol 55, 1377-1394.

Kreisserman, Y., Emmanuel, S., 2018. Release of Particulate Iron Sulfide during Shale-Fluid Interaction. Environ Sci Technol 52, 638-643.

Li, Q., Druhan, J.L., Bargar, J.R., 2022. Influence of sequential stimulation practices on geochemical alteration of shale. Frontiers in Water 4.

Li, Q., Jew, A.D., Kohli, A., Maher, K., Brown, G.E., Bargar, J.R., 2019. Thicknesses of Chemically Altered Zones in Shale Matrices Resulting from Interactions with Hydraulic Fracturing Fluid. Energy & Fuels 33, 6878-6889.

Manz, K.E., Carter, K.E., 2017. Investigating the effects of heat activated persulfate on the degradation of furfural, a component of hydraulic fracturing fluid chemical additives. Chemical Engineering Journal 327, 1021-1032.

Mayhew, L.E., Webb, S.M., Templeton, A.S., 2011. Microscale imaging and identification of Fe speciation and distribution during fluid-mineral reactions under highly reducing conditions. Environ Sci Technol 45, 4468-4474.

Morgan, B., Lahav, O., 2007. The effect of pH on the kinetics of spontaneous Fe (II) oxidation by O2 in aqueous solution–basic principles and a simple heuristic description. Chemosphere 68, 2080-2084.

Palandri, J.L., Kharaka, Y.K., 2004. A compilation of rate parameters of water-mineral interaction kinetics for application to geochemical modeling. Geological Survey Menlo Park CA.

Ravel, B., Newville, M., 2005. ATHENA, ARTEMIS, HEPHAESTUS: data analysis for X-ray absorption spectroscopy using IFEFFIT. Journal of synchrotron radiation 12, 537-541.

Renock, D., Landis, J.D., Sharma, M., 2016. Reductive weathering of black shale and release of barium during hydraulic fracturing. Applied Geochemistry 65, 73-86.

Thompson, J., DeVine, C., 1995. Fracturing fluid interactions with formation minerals and their subsequent effect on formation permeability, SPE Production Operations Symposium. OnePetro.

U.S.EPA, 2015. Analysis of Hydraulic Fracturing Fluid Data from the FracFocus Chemical Disclosure Registry 1.0. Office of Research and Development, Washington, DC. EPA/601/R-14/003.

Vidic, R.D., Brantley, S.L., Vandenbossche, J.M., Yoxtheimer, D., Abad, J.D., 2013. Impact of shale gas development on regional water quality. Science 340, 1235009.

Wang, W., Wei, W., Leach, D., Yan, C., Spilker, K., 2020. Rock-Fluid Interaction and Its Application in Unconventional Production. Unconventional Resources Technology Conference (URTEC).

Webb, S., 2011. The MicroAnalysis Toolkit: X-ray fluorescence image processing software, AIP Conference Proceedings. American Institute of Physics, pp. 196-199.

Xiong, W., Deng, H., Moore, J., Crandall, D., Hakala, J.A., Lopano, C., 2021a. Influence of Flow Pathway Geometry on Barite Scale Deposition in Marcellus Shale during Hydraulic Fracturing. Energy & Fuels 35, 11947-11957.

Xiong, W., Deng, H., Stuckman, M., Lopano, C., Hakala, J.A., 2022a. Fe Oxidation and Species Distribution at the Rock–Fluid Interface of Marcellus Shale Reacted with Hydraulic Fracturing Fluid. Energy & Fuels 36, 8150-8160.

Xiong, W., Gill, M., Moore, J., Crandall, D., Hakala, J.A., Lopano, C., 2020. Influence of Reactive Flow Conditions on Barite Scaling in Marcellus Shale during Stimulation and Shut-In Periods of Hydraulic Fracturing. Energy & Fuels 34, 13625-13635.

Xiong, W., McAdams, B., Stuckman, M., Kutchko, B., Lopano, C., Hakala, J.A., 2022b. The Impact of Hydraulic Fracturing Fluid on the Near-Wellbore Shale Region Involving Interactions with Steel, Cement and Shale, Proceedings of the 10th Unconventional Resources Technology Conference.

Xiong, W., Moore, J., Crandall, D., Lopano, C., Hakala, A., 2021b. Hydraulic Fracturing Geochemical Impact on Fluid Chemistry: Comparing Wolfcamp Shale and Marcellus Shale, Unconventional Resources Technology Conference, 26–28 July 2021. Unconventional Resources Technology Conference (URTeC), pp. 458-470.

# Supplementary Material for < Geochemical Impact of Acid Spearhead and Slick Water Stimulation on Wolfcamp Shale from the Hydraulic Fracturing Test Site>

**Wei Xiong*,** National Energy Technology Laboratory, Pittsburgh, PA 15236, USA**,** NETL Support ContractorPittsburgh, PA 15236, USA; **Hang Deng,** Peking University, Beijing, 100871, China; **Mengling Stuckman**, National Energy Technology Laboratory, Pittsburgh, PA 15236, USA; **Adam Jew,** Stanford Synchrotron Radiation Lightsource, SLAC National Accelerator Laboratory, Menlo Park, CA 94025, USA; **Johnathan Moore,** National Energy Technology Laboratory, Morgantown, WV 26505, USA; **Dustin Crandall,** National Energy Technology Laboratory, Morgantown, WV 26505, USA; **Christina Lopano,** National Energy Technology Laboratory, Pittsburgh, PA 15236, USA; **J. Alexandra Hakala,** National Energy Technology Laboratory, Pittsburgh, PA 15236, USA

**Contents of This File**

- Introduction
- Tables S-1 through S-4
- Figures S-1 through S-4

**Introduction**

This supplementary material includes additional tables and figures that cover the chemistry of the shale; Pre-reaction cores thin section scans; Principle component analysis maps with spot locations for XANES; Spot XANES linear combination fitting analysis; Example of spot XANES analysis with pyrite, ferrihydrite and Fe(III)* XANES; Ca and P XRF maps and the Fe(III)* distribution map, and the correlation analysis of Fe(III)* and Ca; Spot XANES Linear Combination Fitting analysis.

**Table S-1. XRF semi-quantitative analysis of elements in the form of oxides.**

| Core ID/ wt.% | $Al_2O_3$ | $SiO_2$ | $TiO_2$ | $Fe_2O_3$ | MnO | MgO | CaO | $Na_2O$ | $K_2O$ | $P_2O_5$ | Total |
|---|---|---|---|---|---|---|---|---|---|---|---|
| Clay-rich | 12.4 | 71.0 | 0.6 | 3.5 | 0.0 | 1.3 | 1.4 | 0.9 | 2.3 | 0.1 | 93.5 |
| Carb-rich | 3.1 | 22.0 | 0.1 | 6.4 | 0.1 | 4.5 | 20.9 | 0.5 | 0.6 | 0.1 | 58.3 |

**Table S-2. Selected trace element concentrations in the shale.**

| Core ID/ppm | S | Cl | As | Ba | Br | Co | Cr | Cu | Ni | Pb | Sr | Zn | Zr |
|---|---|---|---|---|---|---|---|---|---|---|---|---|---|
| Clay-rich | 2.54 | 0.04 | 3.87 | 241.72 | 7.50 | 0.00 | 174.97 | 43.47 | 134.51 | 27.89 | 163.98 | 234.30 | 127.53 |
| Carb-rich | 0.78 | 0.02 | 1.50 | 107.49 | 4.10 | 12.70 | 62.30 | 15.27 | 27.56 | 0.00 | 552.58 | 77.02 | 45.05 |

**Table S-3. Aqueous chemistry data used for saturation index calculation.**

| | | PITZER database - Day 5 samples | | | Thermo (default) database- Day 5 samples | | |
|---|---|---|---|---|---|---|---|
| Input | Unit | Influent | Clay-rich | Carb-rich | Influent | Clay-rich | Carb-rich |
| Temperature | C | 66 | 66 | 66 | 66 | 66 | 66 |
| pH | pH | 7.01 | 6.32 | 5.95 | 7.01 | 6.32 | 5.95 |
| Fe++ | mg/l | | 2.504 | 9.437 | | 2.504 | 9.437 |
| Co++ | mg/l | 0.01052 | 0.0581 | 0.06343 | 0.01052 | 0.0581 | 0.06343 |
| Ni++ | mg/l | | 3.575 | 8.157 | | 3.575 | 8.157 |
| Cu++ | mg/l | 0.01016 | 0.1513 | 0.2678 | 0.01016 | 0.1513 | 0.2678 |
| Cr+++ | mg/l | | 0.4764 | 1.992 | | 0.4764 | 1.992 |
| Mn++ | mg/l | | 0.6475 | 0.9462 | | 0.6475 | 0.9462 |
| Zn++ | mg/l | | 12.08 | 0.8641 | | 12.08 | 0.8641 |
| Li+ | mg/l | 7.89 | 6.975 | 7.08 | 7.89 | 6.975 | 7.08 |
| Na+ | mg/l | 19549.8 | 17674 | 18479.9 | 19549.8 | 17674 | 18479.9 |
| NH4+ | mg/l | 150.1 | 125.1 | 145.2 | 150.1 | 125.1 | 145.2 |
| K+ | mg/l | 344.3 | 321.5 | 332.4 | 344.3 | 321.5 | 332.4 |
| Mg++ | mg/l | 131.8 | 131.4 | 128.8 | 131.8 | 131.4 | 128.8 |
| Ca++ | mg/l | 868.1 | 795.7 | 832.4 | 868.1 | 795.7 | 832.4 |
| Sr++ | mg/l | 170.8 | 155.3 | 164.2 | 170.8 | 155.3 | 164.2 |
| Cl- | mg/l | 31852.4 | 29936 | 30491.7 | 31852.4 | 29936 | 30491.7 |
| Br- | mg/l | 255.4 | 233.5 | 235.1 | 255.4 | 233.5 | 235.1 |
| NO3- | mg/l | 8.295 | 2.925 | 2.895 | 8.295 | 2.925 | 2.895 |
| SO4-- | mg/l | 831.6 | 972.6 | 993.8 | 831.6 | 972.6 | 993.8 |
| HPO4-- | mmol/l | 0.03134 | 0.02934 | 0.02656 | 0.03134 | 0.02934 | 0.02656 |
| I- | mg/l | 4.594 | 2.55 | 3.228 | 4.594 | 2.55 | 3.228 |
| HCO3- | mg/l (as C) | | | | 49.31 | 37.3 | 26.74 |
| SiO2(aq) | mmol/l (as Si) | | | | 2.03E-04 | 9.98E-04 | 2.12E-04 |
| Output | | | | | | | |
| Dissolved solids | mg/kg | 53605.6 | 49942.1 | 51353 | 53448.6 | 49774.8 | 51110.9 |
| Charge imbalance error | percentage | 0.41% | -1.64% | -0.33% | 0.19% | -1.82% | -0.40% |
| Water type | text | Na-Cl | Na-Cl | Na-Cl | Na-Cl | Na-Cl | Na-Cl |

**Table S-4. Spot XANES linear combination fitting analysis.**

| Clay-Rich | Pyrite | Deviation | Ferrihydrite | Deviation | Fe(III)* | Deviation | Sum | R-Factor |
|---|---|---|---|---|---|---|---|---|
| s1 | 0.197 | 0.016 | 0.81 | 0.016 | | | 1.007 | 0.00572 |

| | | | | | | | | |
|---|---|---|---|---|---|---|---|---|
| s2 | 0.155 | 0.019 | 0.862 | 0.019 | | | 1.018 | 0.00766 |
| s3 | 0.338 | 0.01 | 0.485 | 0.01 | 0.176 | 0.007 | 0.999 | 0.00205 |
| s4 | 0.318 | 0.011 | 0.517 | 0.011 | 0.163 | 0.008 | 0.999 | 0.00261 |
| s5 | | | 0.698 | 0.016 | 0.32 | 0.014 | 1.018 | 0.00933 |
| s6 | | | 0.511 | 0.013 | 0.499 | 0.012 | 1.009 | 0.00655 |
| s7 | | | 0.529 | 0.011 | 0.48 | 0.01 | 1.009 | 0.00453 |
| s8 | | | 0.418 | 0.011 | 0.588 | 0.01 | 1.006 | 0.00495 |
| s9 | | | 0.491 | 0.016 | 0.522 | 0.014 | 1.013 | 0.00937 |
| s10 | 0.894 | 0.007 | | | 0.093 | 0.007 | 0.987 | 0.00257 |
| s11 | 0.248 | 0.012 | 0.248 | 0.012 | 0.493 | 0.008 | 0.989 | 0.00300 |
| s12 | 0.785 | 0.009 | 0.083 | 0.009 | 0.121 | 0.006 | 0.99 | 0.00185 |
| s13 | 0.686 | 0.008 | 0.173 | 0.008 | 0.129 | 0.005 | 0.988 | 0.00140 |
| s14 | 0.089 | 0.014 | 0.266 | 0.014 | 0.637 | 0.01 | 0.993 | 0.00372 |

| Carb-rich | Pyrite | Deviation | Ferrihydrite | Deviation | Fe(III)* | Deviation | sum | R-factor |
|---|---|---|---|---|---|---|---|---|
| s1 | | | 0.503 | 0.016 | 0.501 | 0.014 | 1.003 | 0.009665 |
| s2 | | | 0.412 | 0.016 | 0.607 | 0.015 | 1.019 | 0.009872 |
| s3 | 0.485 | 0.011 | 0.091 | 0.011 | 0.415 | 0.008 | 0.991 | 0.002746 |
| s4 | 0.403 | 0.013 | 0.126 | 0.012 | 0.458 | 0.009 | 0.987 | 0.003271 |
| s5 | | | 0.192 | 0.019 | 0.820 | 0.017 | 1.012 | 0.013193 |
| s6 | | | 0.215 | 0.017 | 0.789 | 0.016 | 1.005 | 0.010854 |

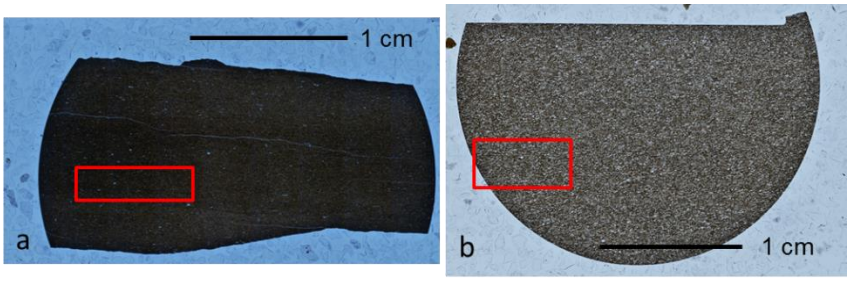


**Figure S-1. Scans of the pre-reaction parent core thin section of a) clay-rich shale and b) carbonate-rich shale. Red boxes are the areas scanned for multi-energy XRF maps.**

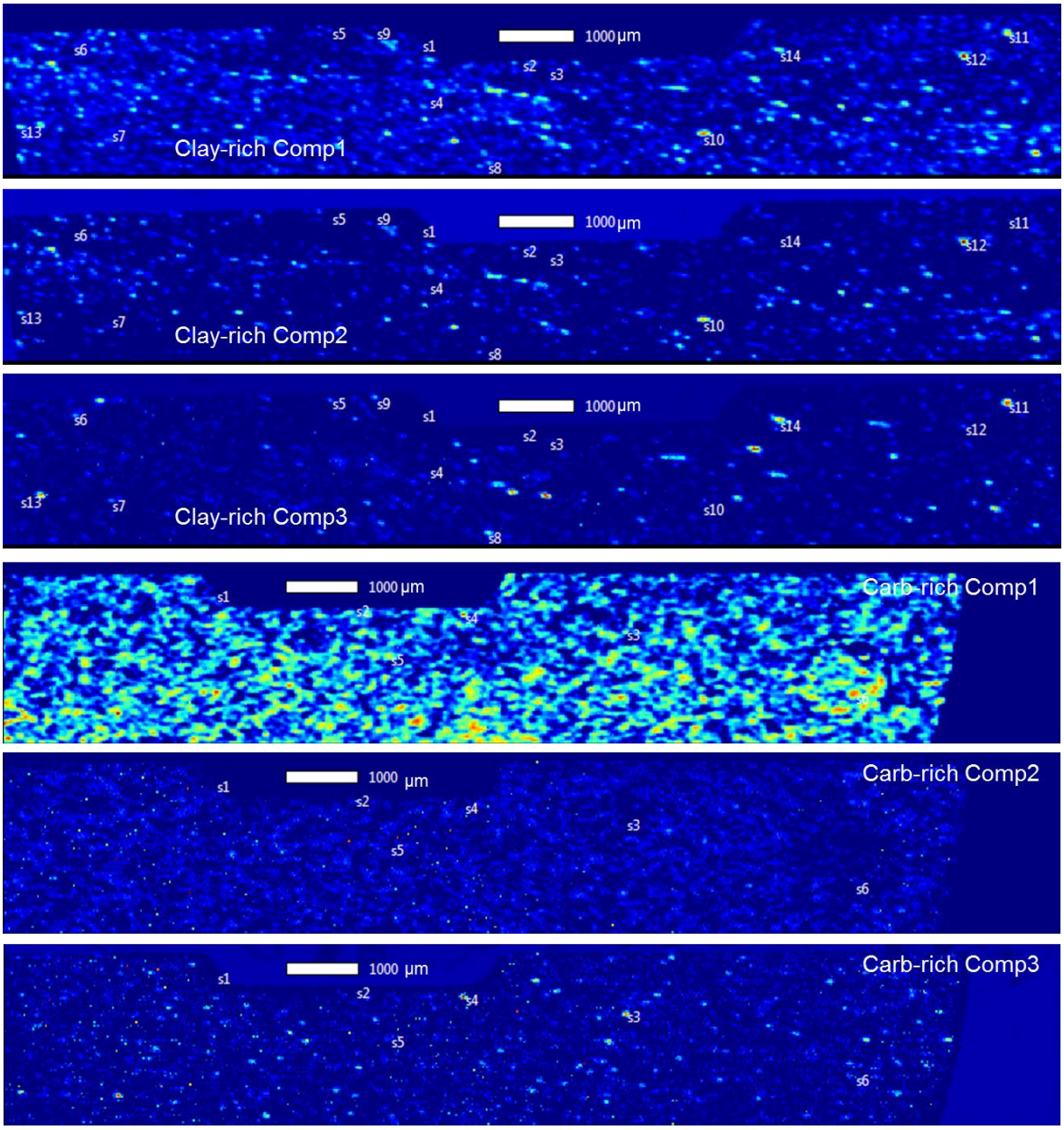


**Figure S-2. Principle component analysis maps with spot locations for XANES.**

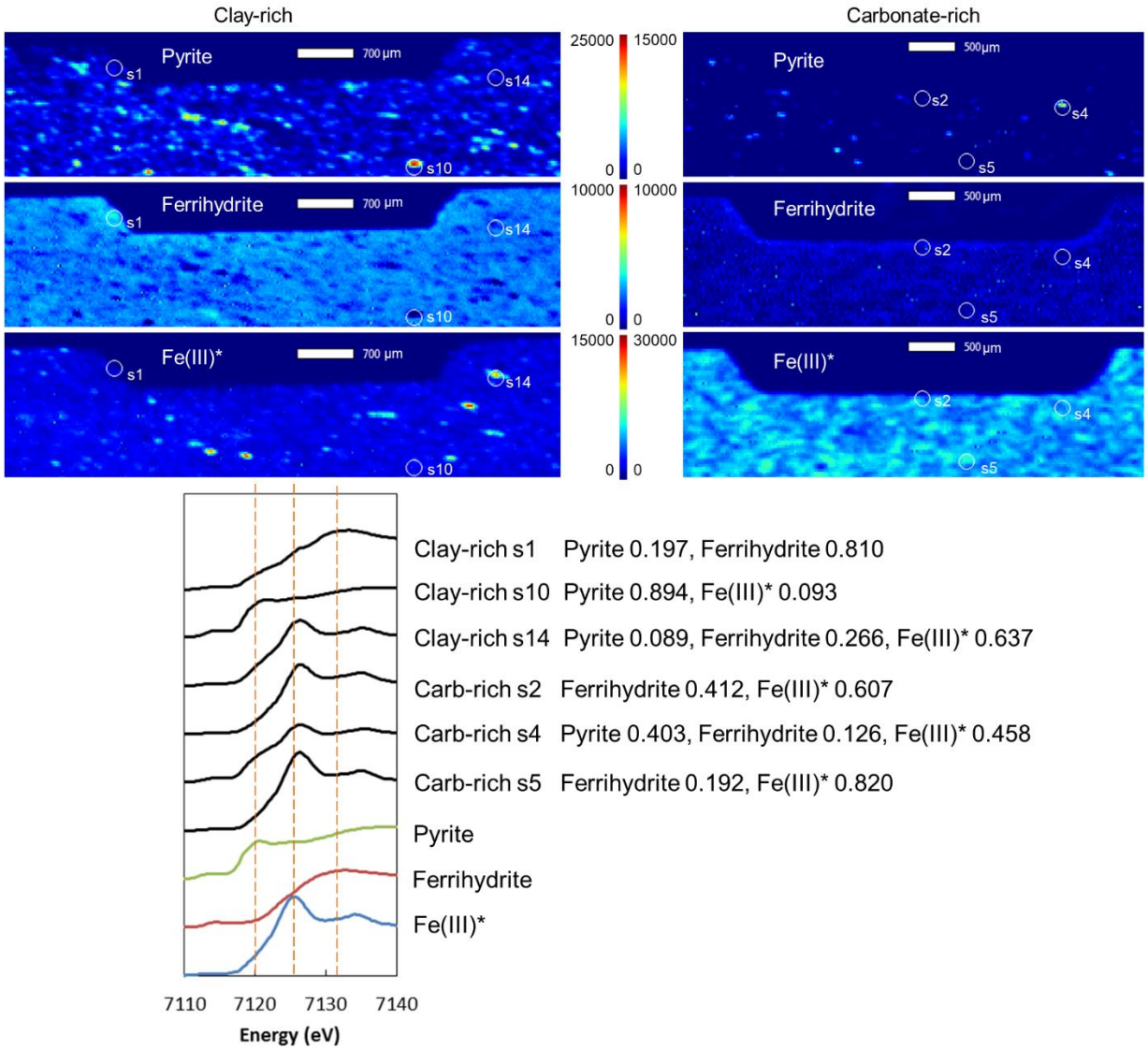


**Figure S-3. Example of spot XANES analysis with pyrite, ferrihydrite and Fe(III)* XANES.**

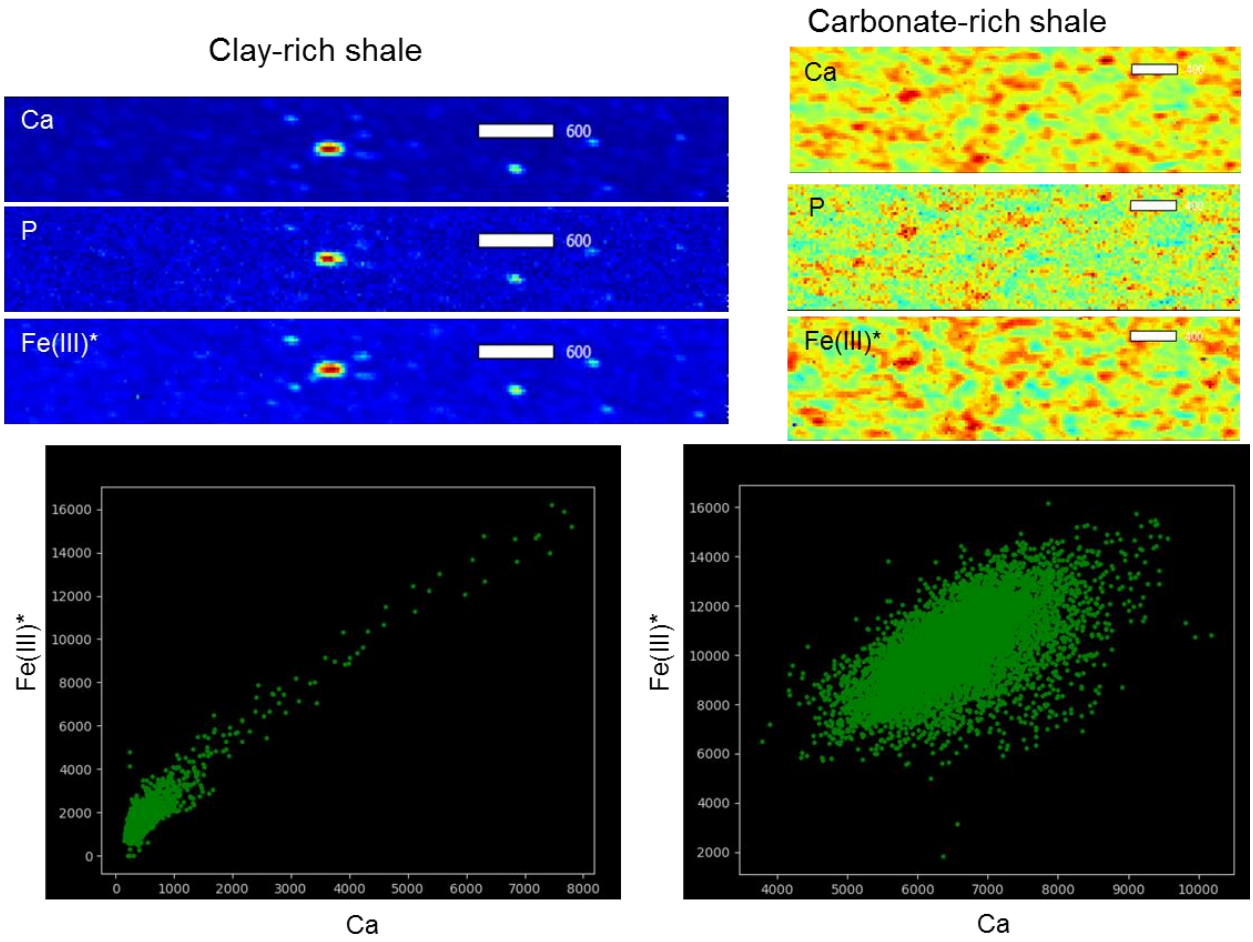


**Figure S-4. Ca and P XRF maps and the Fe(III)* distribution map, and the correlation of Fe(III)* and Ca of the clay-rich and carbonate-rich shale. Scale bar unit is μm.**